🔓 Open Access
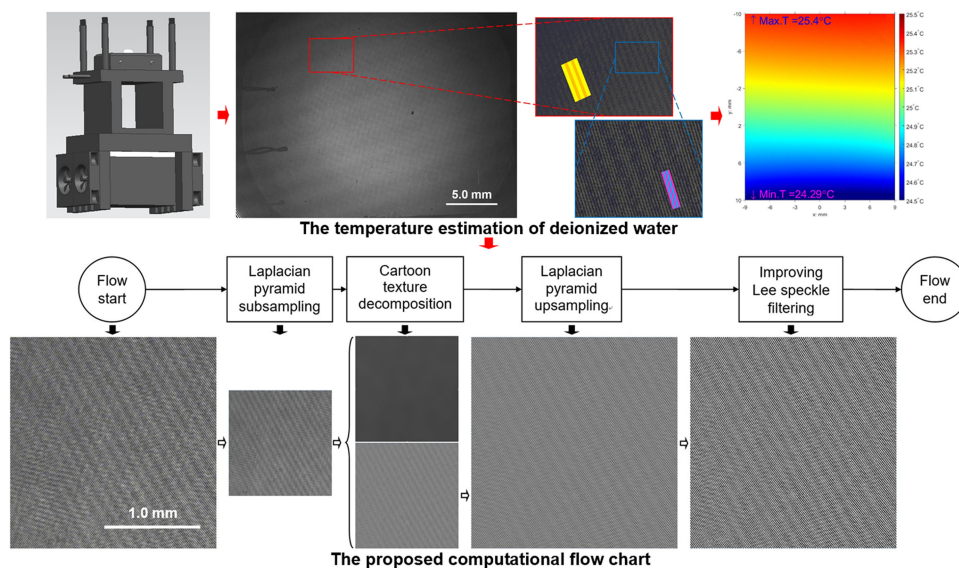
Interference Stripe Noise Reduction of CMOS Sensor-Based Digital Holographic Measurement System

Haoting Liu
Jianyue Ge
Wei Song
Jinhui Lan

The temperature estimation of deionized water

The proposed computational flow chart

IEEE photonics SOCIETY

IEEE

Interference Stripe Noise Reduction of CMOS Sensor-Based Digital Holographic Measurement System

Haoting Liu [iD],[1] **Jianyue Ge** [iD],[1] **Wei Song** [iD],[2] and **Jinhui Lan** [iD][1]

[1]Beijing Engineering Research Center of Industrial Spectrum Imaging, School of Automation and Electrical Engineering, University of Science and Technology Beijing, Beijing 100083, China
[2]Technology and Engineering Center for Space Utilization, Chinese Academy of Sciences, Beijing 100094, China

Abstract: Comparing with the application of charge coupled device (CCD) sensor, a kind of interference stripe noise (ISN) can be observed easily from the complementary metal-oxide-semiconductor (CMOS) sensor-based digital holographic measurement (DHM) system because a series of optic coatings and filters are used in front of that sensor in order to improve its imaging effect. The improper assembly or the micro manufacturing error of these optic components may create the unexpected interference phenomena in the imaging sensor. To reduce that noise, an effective image processing method is developed. On one hand the Laplacian pyramid method is used to highlight the ISN and a cartoon-texture decomposition technique is carried out to remove the additive ISN. On the other hand, an improved Lee filtering is performed to restrain the multiplicative ISN. Extensive experiment results have shown that the image quality can be improved after the ISN reduction and this method is fit for solving a deionized water temperature estimation application where the texture complexity of target image is relatively low.

Index Terms: Digital holographic measurement, CMOS sensor, interference stripe noise, image denoising, temperature estimation.

1. Introduction

The digital holographic measurement (DHM) [1] technique has extensive applications in the concentration diffusion computation, the liquid density estimation [2], and the particle movement test [3], etc. Fig. 1 presents a kind of optical path sketch map of DHM system. In Fig. 1, in contrast to the traditional optical path [4] which always chooses to use the charge coupled device (CCD) sensor to collect the interference beams, the complementary metal-oxide-semiconductor (CMOS) sensor [5] is utilized. Clearly, the cost of CMOS is cheaper, and its low power consumption and fast processing speed also determine its first-choice status in some typical applications. For example, a CMOS sensor-based DHM system is now being developed for the thermal analysis research in China space station. However, because the CMOS sensor uses the signal amplifier in its each
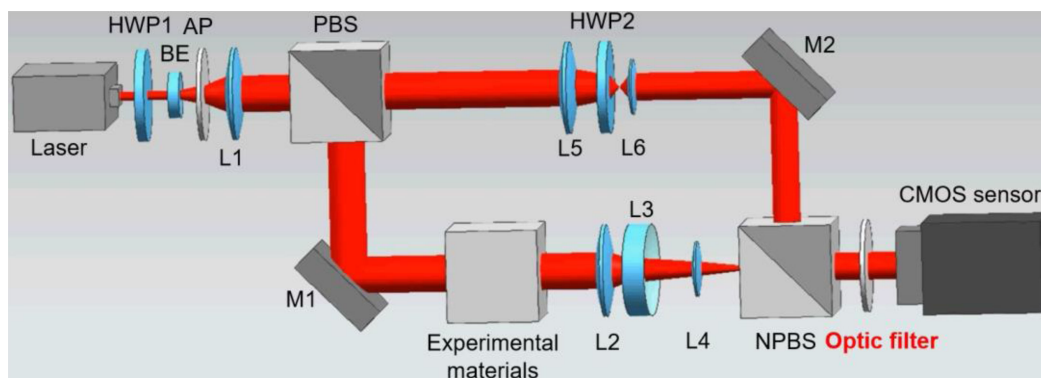
Fig. 1. The optical path sketch map of proposed DHM system. The HWP is the half-wavelength plate; the BE is the beam expander; the AP is the aperture; the L is the lens; the PBS is the polarized beam splitter; the NPBS is the non-polarized beam splitter; and the M is the mirror.

sensor unit [6], its imaging effect will not be as good as that of the CCD sensor. To conquer that problem, a series of optic processes and optic components, e.g., the optic coating technique and the optic filter, are used for it. Inevitably, the application of these complex optic components will cause some potential problems. In many cases, the unparallel assembly of the optic filter and the CMOS sensor, or the micro machining error of optic component will lead to an abnormal light transmission in the DHM system, and some new interference phenomena will occur in the sensor surface. These new interference stripes can be looked on as the noises and should be reduced.

According to the digital holographic theory [7], a physical field can be deduced and reconstructed by analyzing the interference stripes. Equation (1) presents its ideal computational model. The processing steps of DHM system include the image preprocessing, the complex amplitude map computation, and the phase unwrapping, etc. In practice, many noises [8] will affect the imaging effect of DHM. The familiar noises include the system noises and the random noises. The system noises [9] mainly come from the improper light source or the assembly error of optic path. The random noises [10] always point to the unexpected disturbances which are derived from the optic or the electronic components. From the digital image processing point of view, these noises above can also be written as the additive noise and the multiplicative noise. Equation (2) shows its model. Many methods [11] have been developed to solve these additive or multiplicative noises. For example, in [12], the authors utilized an aperture function matching method and a Wiener filtering to reduce the multiplicative noise. In [13], an interpolation-based algorithm was developed to reduce both the additive and the multiplicative noises. Currently, the researches about the noise reduction issue of the CMOS sensor-based DHM system are still rare; and both the additive and the multiplicative noises should be considered in this system.

$$I_{ide}(x, y) = \left| O(x, y) + R(x, y) \right|^2 \tag{1}$$

$$I_{sen}(x, y) = f_n(x, y) \times I_{ide}(x, y) + v_n(x, y) \tag{2}$$

where $I_{ide}(x, y)$ is the ideal holographic imaging result; $O(x, y)$ is the object beam; and $R(x, y)$ represents the reference beam; $I_{sen}(x, y)$ is the practical output of imaging sensor; $f_n(x, y)$ is the multiplicative noise function and $v_n(x, y)$ is the additive noise function.

Fig. 2 presents the sketch map of CMOS sensor and a DHM image sample. In Fig. 2, (a) is the sketch map of CMOS sensor. It includes the infrared radiation filter, the lens elements, and some other micro lenses, etc. More applications of the optic components will lead to the unexpected imaging errors comparing with the case of CCD sensor [14]. Fig. 2(b) shows an imaging example captured from the CMOS sensor-based DHM system. An application of the temperature measurement of deionized water is presented here. From Fig. 2(b), a kind of coarse interference stripe noise (ISN) can be observed in the image clearly which is marked by a yellow-orange stripe group. The normal interference stripe [15] is also annotated by a pink-blue stripe group in its sub-image.
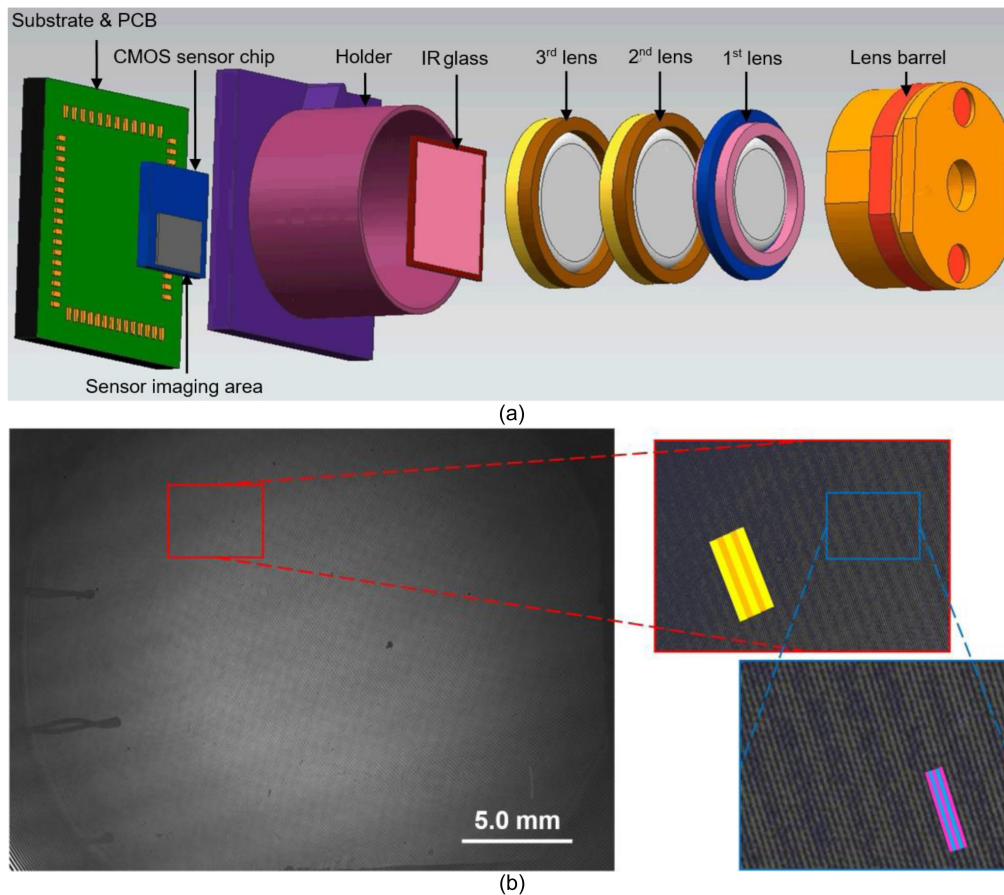
(a)

(b)

Fig. 2. The sketch map of CMOS sensor and its imaging sample. (a) The sketch map of CMOS sensor. (b) The image sample of the temperature measurement of deionized water.

It should be emphasized the widths between any two neighboring yellow-orange stripes may not be equal; while the ideal pink-blue stripe should have an equal-spaced distribution. In this system, when the installation direction of optic filter is not parallel to the CMOS sensor strictly, the reflections of the object beams and the reference beams between the filter and the sensor surface will happen; this will lead to the new interference phenomena and create the ISNs. In other case, if the planeness or the transmittancy of the optic coating or the optic filter is not uniform, the transmissions of object beams and reference beams will also deviate their designed paths; as a result the ISNs may also be generated. Clearly, the ISN will affect the following computations, such as the phase unwrapping or the gradient estimation. After a series of tests it can be found the ISNs always have the additive components and the multiplicative ones; therefore it is necessary to design an integrated method to reduce them.

2. Proposed ISN Reduction Method

2.1 Computational Flow Chart

To restrain the ISN, an image processing method is developed. Fig. 3 illustrates our proposed computational flow chart. The corresponding image processing examples are also presented. First, the Laplacian pyramid subsampling [16] is used to highlight the ISN. Because the width of ISN is larger than the width of the normal interference stripe; after the subsampling, the ISN still can be retained while the normal stripe will be protected to some extent. The Laplacian
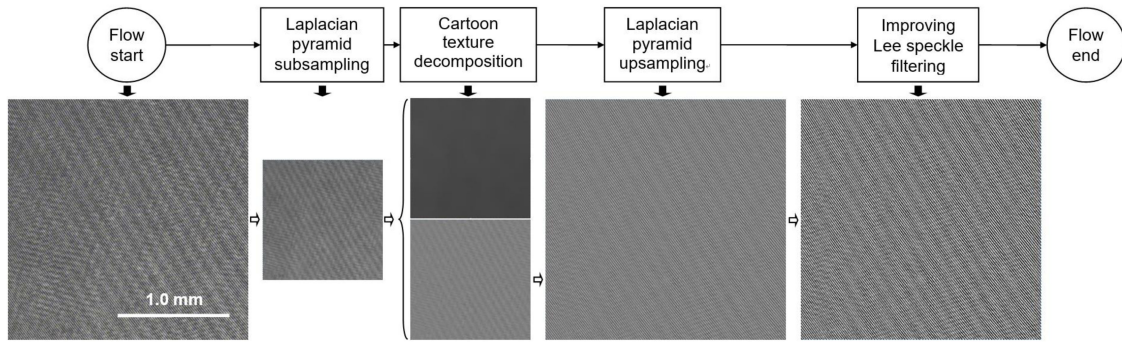
Fig. 3. The proposed computational flow chart.

pyramid is used here because it can not only decrease the resolution of holographic image but also keep the image edge well. Second, a kind of cartoon-texture decomposition [17] is considered to reduce the additive ISN. The cartoon-texture decomposition can separate the image into a cartoon part and a texture part. In our application, both the image background and the additive ISN belong to the cartoon part; while the normal interference stripe is classified as the texture part. Third, the Laplacian pyramid upsampling is performed to the texture part. Finally, an improved Lee filtering is implemented to restrain the multiplicative ISN furtherly. The improved Lee filter is developed because it can process the multiplicative noise [18] well and avoid the excessive edge enhancement. After the ISN reduction, the processed image can be used for the following computations, such as the fast Fourier transform (FFT) and the phase unwrapping, etc.; and the gradient can also be estimated more accurately by using our method.

2.2 Computational Details

Without loss of generality, let us take the ISN reduction of the deionized water image as an example to explain our method in details. The Laplacian pyramid is used to decrease the resolution of original holographic image firstly. This step can highlight the ISNs. If the original image is written by I_0, it can be looked on as the top level of a Gaussian pyramid; and then the lth level of the Gaussian pyramid can be computed by (3). Then the Laplacian pyramid can be defined by the difference between the lth Gaussian pyramid and its interpolation result of the (l-1)th level. The corresponding computational methods are shown by (4) to (6). In our application, because the widths of ISN are about 8 to 12 pixels, and the image size will be reduced to one fourth of its former level after each pyramid operation; as a result the Laplacian pyramid computation will be performed only for once. Fig. 4(a) presents the original holographic image, (b) shows the subsampling result of Laplacian pyramid, and (c) illustrates the residual image after the Laplacian pyramid processing. When computing the residual image, first, the original image is processed by the Laplacian pyramid subsampling; second, an upsampling of Laplacian pyramid will be implemented immediately; and third, we will use the original image to subtract the upsampling result to get the residual image. Clearly, from (c), some information will be lost after the Laplacian pyramid computation; however we think the lost information mainly belong to the background after the careful observation of the residual image.

$$I_l = \sum_{m=-2}^{2} \sum_{n=-2}^{2} w\,(m, n)\, I_{l-1}\,(2i + m, 2j + n) \tag{3}$$

$$\begin{cases} LP_l = I_l - I_{l-1}^* & 0 \le l < N \\ LP_N = I_N & l = N \end{cases} \tag{4}$$
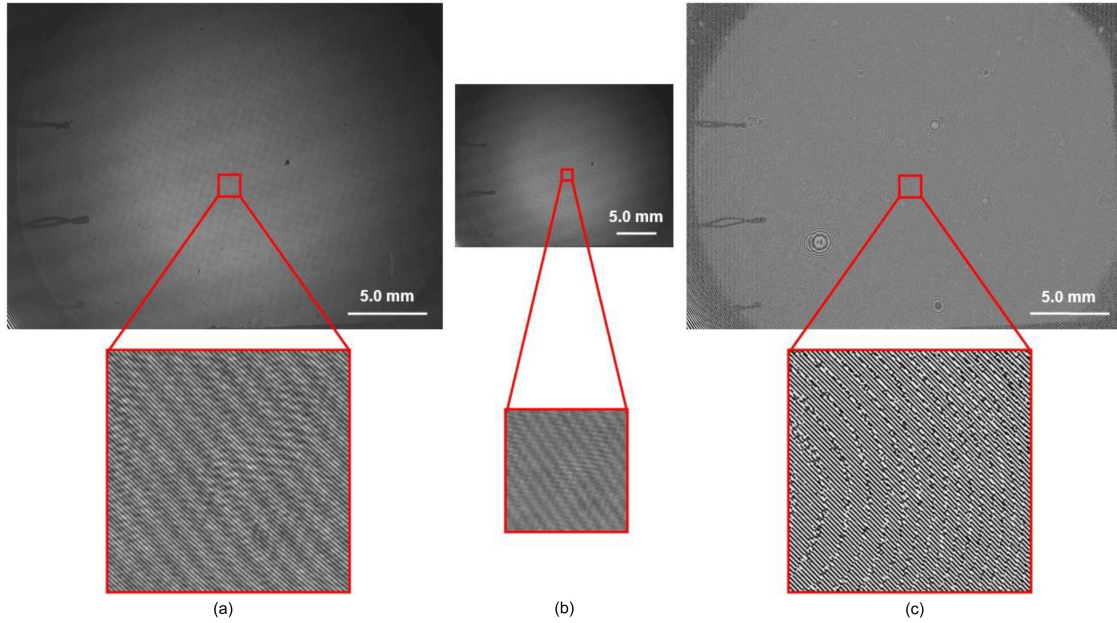
Fig. 4. The Laplacian pyramid processing results of proposed algorithm. (a) The original holographic image. (b) The Laplacian pyramid subsampling result of (a). (c) The residual image of (b).

$$I_l^*(i, j) = 4 \sum_{m=-2}^{2} \sum_{n=-2}^{2} w(m, n) I_l^* \left(\frac{i+m}{2}, \frac{j+n}{2} \right) \tag{5}$$

$$I_l^* \left(\frac{i+m}{2}, \frac{j+n}{2} \right) = \begin{cases} I_l \left(\frac{i+m}{2}, \frac{j+n}{2} \right) & \frac{i+m}{2}, \frac{j+n}{2} \in Z \\ 0 & otherwise \end{cases} \tag{6}$$

where $1 \leq l \leq N$, $0 \leq i \leq R_l$, and $0 \leq j \leq C_l$; N is the top level number of Gaussian pyramid, R_l and C_l are the row number and the column number of Gaussian pyramid; $w(m, n)$ is a window function of low pass filter; LP_N is the top level image of Laplacian pyramid; LP_l is the lth decomposition result of Laplacian pyramid.

The cartoon-texture decomposition is employed to separate the image into the background part with ISN and the normal interference stripe part. In general, the cartoon-texture decomposition uses a typical additive noise model to represent the whole image, i.e., this method thinks an image includes a coarse outline, a detailed texture, and some noises. The outline and the texture belong to the low and the high frequency signals, respectively; while the noises can be observed in both the cartoon part and the texture part. A total variation-based method is utilized to implement the cartoon-texture decomposition in this paper. The total variation-based method transforms the image denoising problem into a functional minimization solution issue by using the Lagrange's method of undetermined multiplier and the gradient descent technique. Since it is very hard to distinguish the cartoon part and the texture part, i.e., a simple high pass or low pass filter cannot work, a linear weighted computational strategy is considered here: a parameter (Equation (7)) which can represent the texture intensity is defined; and the cartoon part (Equations (8) and (9)) can be calculated by the weighted sum of the image after a low pass filter and the product of the original image and a texture intensity parameter. After the additive ISN is reduced, the upsampling of Laplacian pyramid will be performed. Equation (10) is its computational method. Fig. 5 shows the corresponding computational results of cartoon-texture decomposition and Laplacian pyramid up-sampling. In Fig. 5, (a) and (b) illustrate the cartoon and the texture parts of Fig. 4(b), respectively;
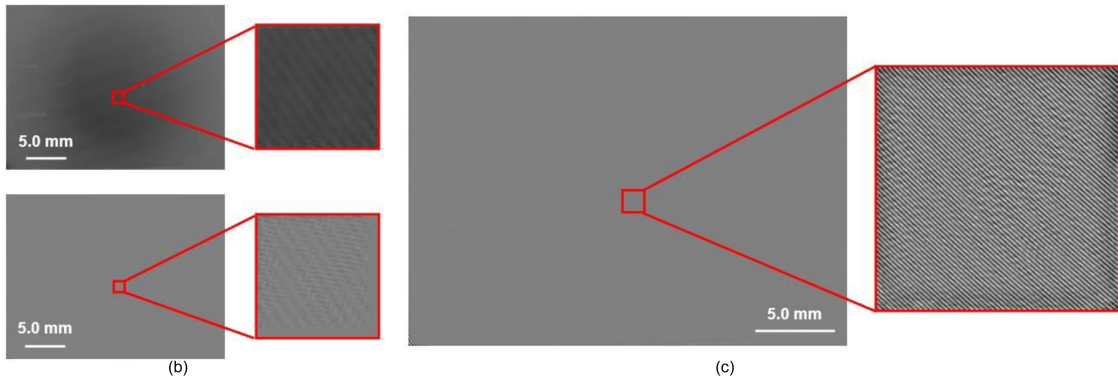
Fig. 5. The processing results of cartoon-texture decomposition and Laplacian pyramid upsampling. (a) The cartoon part of Fig. 4(b). (b) The texture part of Fig. 4(b). (c) The result of Laplacian pyramid upsampling of Fig. 5(b).

and Fig. 5(c) presents the Laplacian pyramid upsampling result of Fig. 5(b).

$$\rho = \frac{G_\sigma * |\nabla I'| - G_\sigma * |\nabla (L_\sigma * I')|}{G_\sigma * |\nabla I'|} \tag{7}$$

$$\begin{cases} Car = f(\rho)(L_\sigma * I') + [1 - f(\rho)] I' \\ Tex = I' - Car \end{cases} \tag{8}$$

$$f(x) = \begin{cases} 0 & x \le T_1 \\ ax + b & T_1 < x < T_2 \\ 1 & x \ge T_2 \end{cases} \tag{9}$$

$$\begin{cases} I'' = G_N = LP_N & l = N \\ G_l = LP_l + G^*_{l+1} & 0 \le l < N \end{cases} \tag{10}$$

where I' is the output of the Laplacian pyramid subsampling, and $I' = LP_1$; G_σ is a Gaussian kernel function, σ is its standard deviation, $\sigma = 5$; symbol "∇" means the gradient operator; symbol "$*$" means the convolution processing; L_σ is a low pass filter; ρ represents the relative reduction rate of the local total variation; $f(x)$ is a piecewise linear function; Car and Tex mean the cartoon part and the texture part of image, respectively; T_1 and T_2 are thresholds, $T_1 = 0.25$, $T_2 = 0.5$; a and b are the variables of function $f(x)$, $a = 4$, $b = -1$; I' is the output of Laplacian upsampling.

The multiplicative noise should also be restrained from the DHM image. Actually, in many cases the multiplicative noise is more dominant in the DHM image. An improved Lee filter is developed in this paper. The classic Lee filter is a tool which can reduce the noises that have some typical distribution modes. It can be computed by using the smooth region of an image to estimate the noise priors. However, the practical DHM image is more complex and it has both the smooth region and the complex texture part. To improve the processing effect of Lee filter, in this paper, all the pixels in image are classified as the intensity smoothness pixel, the intensity change one (i.e., the edge pixel), and the middle one. Then different denoising strategies are employed to these pixels to carry out the Lee filter. Equations (11) to (16) illustrate the computational method of improved Lee filtering. From these equations, a ratio between the image variance and the image mean is used to evaluate the pixel intensity state; two thresholds are considered to distinguish the pixel type. Clearly, the proposed computational method can avoid the over enhancement problem in image. The over enhancement means the difference between the detail and the background is too significant and goes beyond their essential diversity scopes. Fig. 6 shows the result of improved Lee filter. Comparing with Fig. 4(a), most of the image background and ISNs are reduced from
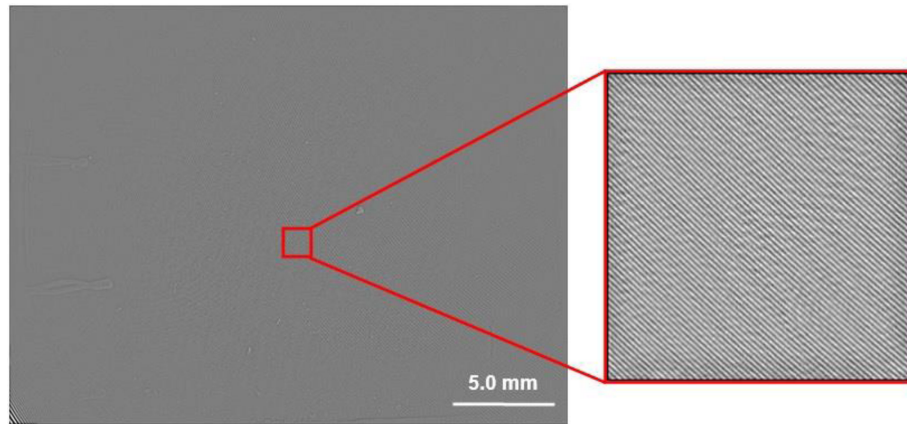
Fig. 6. The processing result of improved Lee filtering.

image, and the normal interference stripes can be kept to some extent.

$$I''' = \begin{cases} I'''_{est} & C_l \leq C_u \\ I'''_{est} + k\left(I'' - I'''_{est}\right) & C_u < C_l \leq C_m \\ I'' & C_l > C_m \end{cases} \tag{11}$$

$$I'''_{est} = mean\left(I''\right) / mean\left(N_{Mul}\right) \tag{12}$$

$$C_l = var\left(I'''_{est}\right) / mean\left(I'''_{est}\right) \tag{13}$$

$$C_u = K \Big/ \sqrt{mean^2\left(I''\right) / var\left(I''\right)} \tag{14}$$

$$C_m = C_u \sqrt{1 + 2/\left[mean^2\left(I''\right) / var\left(I''\right)\right]} \tag{15}$$

$$k = \frac{var\left(I'''_{est}\right)}{mean^2\left(I'''_{est}\right) var\left(N_{Mul}\right) + var\left(I'''_{est}\right)} \tag{16}$$

where I''_{est} is the estimation of I''; k is a weight; function $mean(x)$ is to compute the mean value of variable x; $var(x)$ is to calculate the variance of variable x; N_{Mul} is a multiplicative noise; K is a parameter, $K = 0.5227$; C_I, C_u, and C_m are the thresholds.

3. Experiments & Discussions

Seven ISN reduction algorithms are compared in this paper to assess the effects of image processing methods, they are: the cartoon texture filter-based method (named as method 1), the Laplacian pyramid + the cartoon texture-based method (named as method 2), the Laplacian pyramid + cartoon texture + Frost filter [19]-based method (named as method 3), the Laplacian pyramid + cartoon texture + Gamma filter [20]-based method (named as method 4), the Laplacian pyramid + cartoon texture + Lee filter [21]-based method (named as method 5), the Laplacian pyramid + cartoon texture + improved Lee filter + angular spectrum filter [22]-based method (named as method 6), and the Laplacian pyramid + cartoon texture + improved Lee filter method (our method). Two experiments are designed to evaluate the performance of proposed ISN reduction algorithm. In the first experiment, because the gray level co-occurrence matrix (GLCM) can assess the texture details synthetically [23], its eight features are considered, i.e., the entropy M_{G_ENT}, the contrast M_{G_CON}, the angular second moment M_{G_ASM}, the inverse different moment M_{G_IDM}, the difference variance $M_{G\_D\_VAR}$, the average gradient M_{G_AG}, the information measure of correlation 2 M_{G_IMC2}, and the maximum probability $M_{G \cdot MP}$. In the second experiment, the proposed method is

TABLE 1
The Main Performance Parameters of CMOS Sensor

Chip size (mm × mm)	Resolution (pixel × pixel)	Pixel size (μm × μm)	Frame speed (fps)	Mono / Color	Quantum efficiency	Dynamic range (dB)	Signal noise ratio (dB)
14.1×10.3	4096×3000	3.45×3.45	8	Mono	≈70%	72.8	40.2

TABLE 2
Results of Image Quality Evaluation Experiment Using Different ISN Reduction Methods

		ISN reduction methods							
		Original image	Method 1	Method 2	Method 3	Method 4	Method 5	Method 6	Our method
GLCM features	M_{G_ENT}	2.5450	2.2058	2.3176	1.0821	2.1672	2.8975	3.44636	**3.44641**
	M_{G_CON}	0.8288	0.8531	0.9855	0.2432	0.8064	1.2825	1.2825	**3.0221**
	M_{G_ASM}	0.1166	0.1629	0.1330	0.5421	0.1815	0.1101	0.1100	**0.0533**
	M_{G_IDM}	0.7282	0.7344	0.6847	0.8910	0.7666	0.7354	0.6371	**0.5809**
	$M_{G\_D\_VAR}$	0.8288	0.8531	0.9856	0.2432	0.8064	1.2825	1.2826	**3.0221**
	M_{G_AG}	23.5935	11.8096	20.0710	6.1329	14.4901	28.1244	42.2556	**48.2517**
	M_{G_IMC2}	0.6892	0.3345	0.2284	0.3032	0.4209	0.7022	0.7021	**0.8781**
	M_{G_MP}	0.2443	0.3326	0.2070	0.7267	0.3488	0.2439	0.2522	**0.1302**

used to estimate the temperature field of deionized water. An experimental system is developed and a comparison is also made between our computation result and the thermocouple measurement result. When building the DHM system, a Helium-neon gas laser with 632.8 nm wavelength is used. The main parameters of the CMOS sensor (manufacturer: Basler) are illustrated in Table 1. All the simulation programs are written by Python 3.7 on our PC (Intel Core^{TM} i7, 8GB RAM).

3.1 The Evaluation Experiment of Image Quality

Regarding the first experiment, eight GLCM features are used. The entropy M_{G_ENT} can represent the information content of an image; the larger the entropy is, the bigger the information amount will be. The contrast M_{G_CON} can indicate the difference between the image foreground and background; the larger the contrast is, the clearer the image detail will be. The angular second moment M_{G_ASM} can show the intensity distribution uniformity of image; the smaller the angular second moment is, the finer the texture will be. The inverse different moment M_{G_IDM} can illustrate the image texture uniformity; the smaller the inverse different moment is, the more uniform the texture will be. The difference variance $M_{G\_D\_VAR}$ can reflect the periodic texture intensity; the larger the difference variance is, the denser the texture will be. The average gradient M_{G_AG} can mean the image definition; the larger the average gradient is, the bigger the image definition will be. The information measure of correlation 2 M_{G_IMC2} can hint the texture homogeneity; the larger the information measure of correlation 2 is, the better the texture homogeneity will be. And the maximum probability M_{G_MP} can give out the occurrence probability of the most familiar texture in an image; the smaller the maximum probability is, the better the image texture consistency will be. Table 2 presents the computational results of GLCM features using different ISN reduction
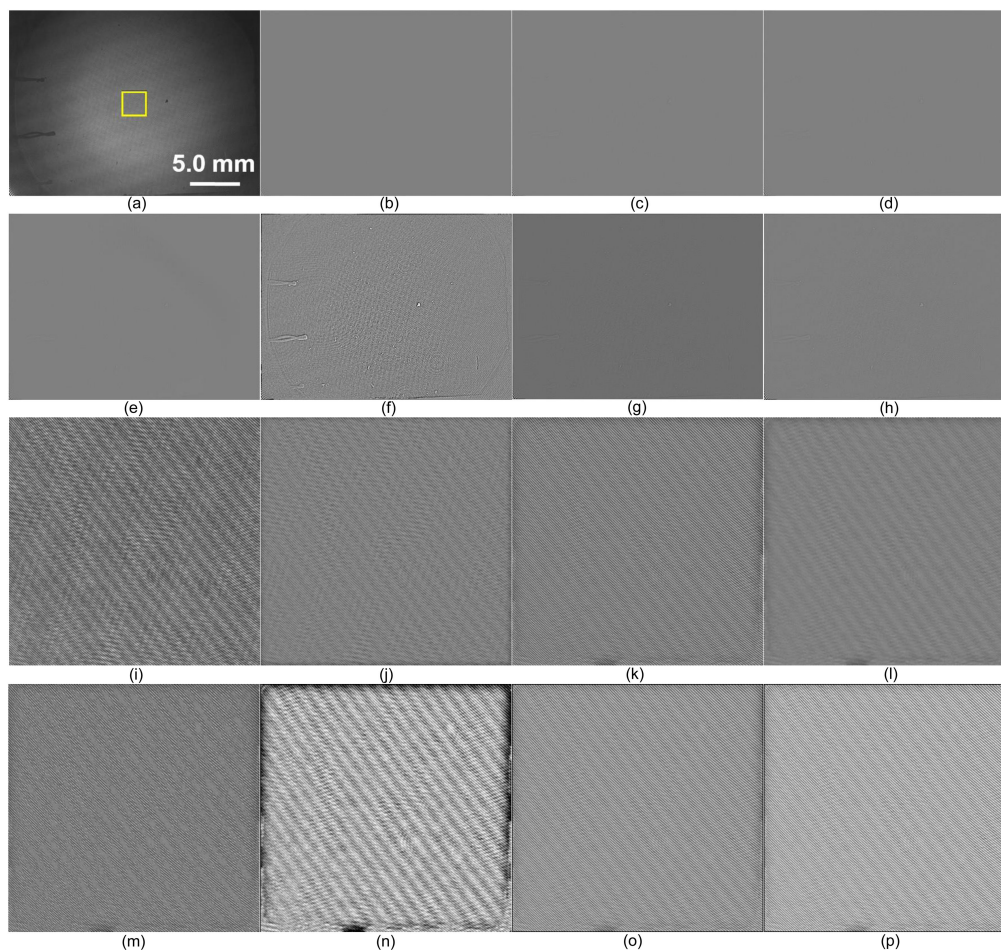
Fig. 7. The results using different noise reduction methods. (a) The original holographic image. (b) The result using method 1. (c) The result using method 2. (d) The result using method 3. (e) The result using method 4. (f) The result using method 5. (g) The result using method 6. (h) The result using our method. (i) The local enlarged image of (a). (j) The local enlarged image of (b). (k) The local enlarged image of (c). (l) The local enlarged image of (d). (m) The local enlarged image of (e). (n) The local enlarged image of (f). (o) The local enlarged image of (g). (p) The local enlarged image of (h).

methods. The best values are marked in boldface. From Table 2, our proposed method can achieve the best processing effect.

Fig. 7 shows the image processing results using different ISN reduction methods. In Fig. 7, (a) is the original DHM image, and (b) to (h) illustrate the results corresponding to the methods presented in Table 2. To illustrate the imaging details clearly, the enlarged versions of (a) to (h) are shown in (i) to (p), respectively. The sampling position of (i) to (p) is marked in (a) by a yellow rectangle. From these results, the ISN can be observed in Fig. 5(i) clearly. The methods in (j), (k), and (l) can restrain the ISN to some extent; however their processing effects are limited according to the analysis results of image quality in Table 2. The result in (m) can eliminate the ISN effectively; unfortunately, the normal stripes are also destroyed seriously. The result in (n) which uses the traditional Lee filter meets the over enhancement problem; the enhanced texture edges will affect the following gradient computation. The result in (o) adds an additional processing step comparing with our method, i.e., the angular spectrum filter is considered; however, this method cannot improve the processing effect according to the results of image quality. This result may be explained that the angular spectrum filter cannot locate and eliminate the ISN frequency spectrum accurately. From

Fig. 7 and Table 2, our method can achieve the best computational effect. After the ISN reduction, the image quality can be improved which means more useful image details are kept and enhanced.

3.2 The Evaluation Experiment of Deionized Water Temperature Estimation

The second experiment utilizes the noise reduction image above to estimate the temperature of deionized water. The research of a precise fluid temperature measurement in the microgravity environment is meaningful for the method study of space station thermal control technique; thus a prototype experiment device is developed. Fig. 8(a) presents the sketch map of that device. In Fig. 8(a), a sealing box is designed to retain the deionized water. The coated glasses are used as its two sides so that the object beams and reference beams can pass through these sides. A heating component and a refrigeration component are installed at the top and the bottom of that sealing box, respectively, which can create a non-buoyancy convection environment [24]. And then the temperature gradient field of deionized water can be looked on as a multi-layer and stable fluid distribution. Approximatively, the water in the same spatial height will have the same temperature in this system. A thermocouple sensor is employed to measure the practical water temperature, and it can be inserted in different places of that metal sealing box. In this experiment it is only installed at the top of that box. The holographic image is used to estimate the water temperature in this paper. After the ISN reduction, the image will be transformed into the frequency domain by FFT, the selection of the $+1$ level component and the phase unwrapping computation will be performed, then the temperature field image can be gotten. Fig. 8(b) is an original digital holographic image; (c) presents the result after ISN reduction using our proposed method; (d) is the intensity image of (c) after FFT computation; (e) is the segmentation result of the $+1$ level component of (d); (f) is the wrapped phase image of (e); (g) is the phase unwrapping result of (f); and (h) is the final visual image of temperature field. Equation (17) presents the relationship function between the water refractivity and the DHM phase information. According to the Lorentz-Lorenz equation and its corresponding theories [25], the relationship between the water refractivity and the temperature can be described by a polynomial function [26]. After a series of pre-experiments, the function (18) is used in our experiment. And the analytic solutions of (18) can be computed by the equations (19) to (22) [27].

$$n(x, y) = \frac{\lambda \Delta \varphi_{obj}(x, y)}{2\pi d_0} + n_0 \tag{17}$$

$$n = aT^3 + bT^2 + cT + n_c \tag{18}$$

$$T = t - \frac{b}{3a} \tag{19}$$

$$t^3 + pt + q = 0 \tag{20}$$

$$p = \frac{3ac - b^2}{3a^2} \tag{21}$$

$$q = \frac{2b^3 - 9abc + 27a^2(n_c - n)}{27a^3} \tag{22}$$

where $n(x, y)$ is the refractivity distribution; λ is the wavelength of laser, $\lambda = 632.8$ nm; $\Delta \varphi_{obj}(x, y)$ is the phase distribution information; d_0 is the propagation distance of object beam in water, $d_0 \approx$ 30.0 mm; n_0 is refractivity of deionized water when the initial temperature is 25.2 °C, $n_0 = 1.3316$; n is the refractivity; a_0, a_1, and a_2 are the weights, $a = 5.0 \times 10^{-9}$, $b = -2.0 \times 10^{-6}$, and $c = -1.0 \times 10^{-5}$; n_c is a constant, $n_c = 1.3331$; p and q are the intermediate variables.

Fig. 9 illustrates the comparison results of temperature estimation experiment using the thermocouple measurement method and the DHM computation techniques. Different ISN reduction algorithms are compared in this experiment. Table 3 presents the main performance parameters of the thermocouple device (manufacturer: Omega). In Fig. 9, (a) shows a temperature comparison
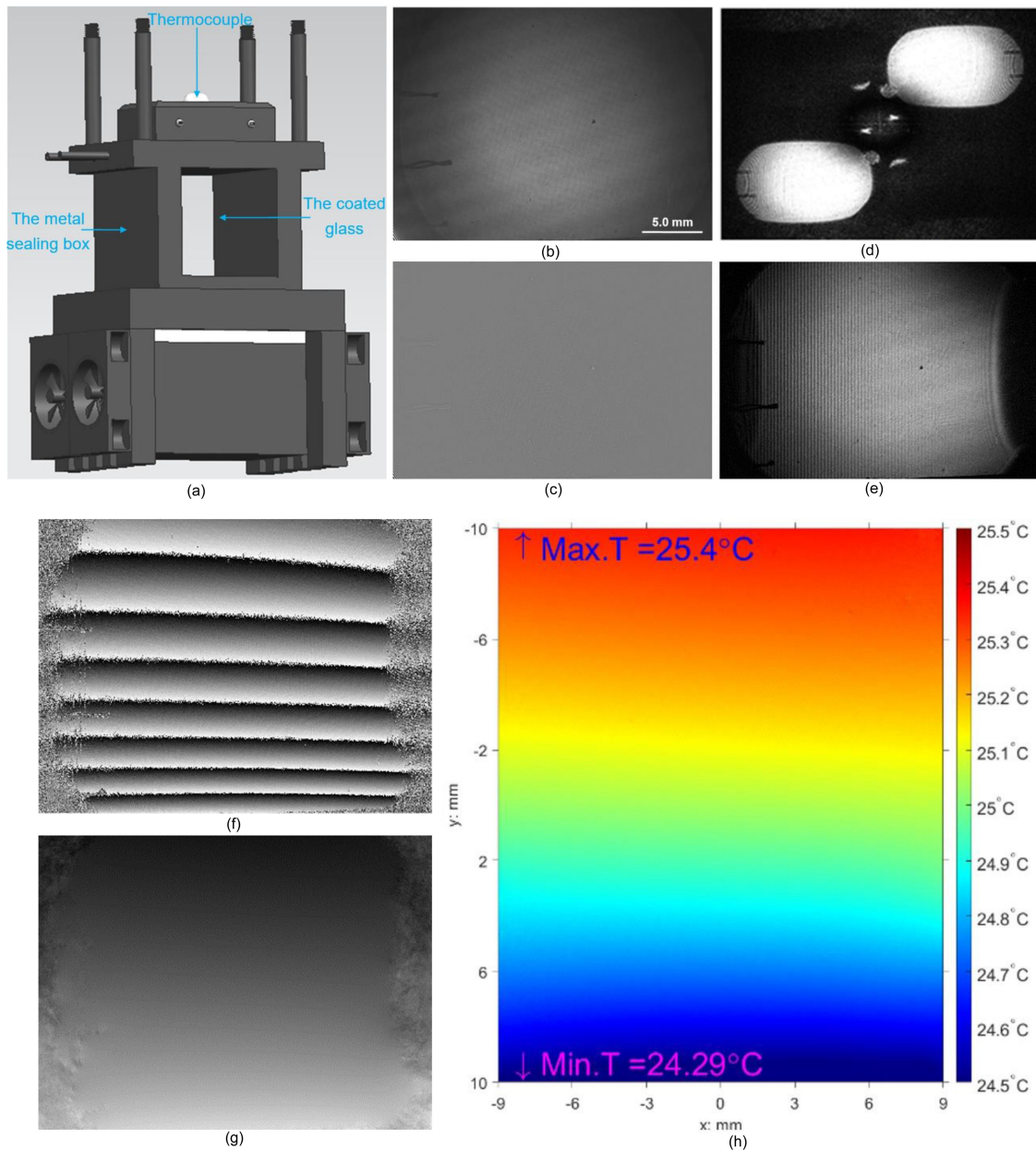
Fig. 8. The sketch map of temperature measurement experiment system and the corresponding results. (a) The sketch map of the deionized water sealing box. (b) The original digital holographic image. (c) The ISN reduction result of (b) using our proposed method. (d) The FFT result of (c). (e) The segmentation result of +1 level component of (d). (f) The wrapped phase image of (e). (g) The phase unwrapping result of (f). (h) The reconstruction result of temperature field.

TABLE 3
The Main Performance Parameters of Thermocouple Sensor

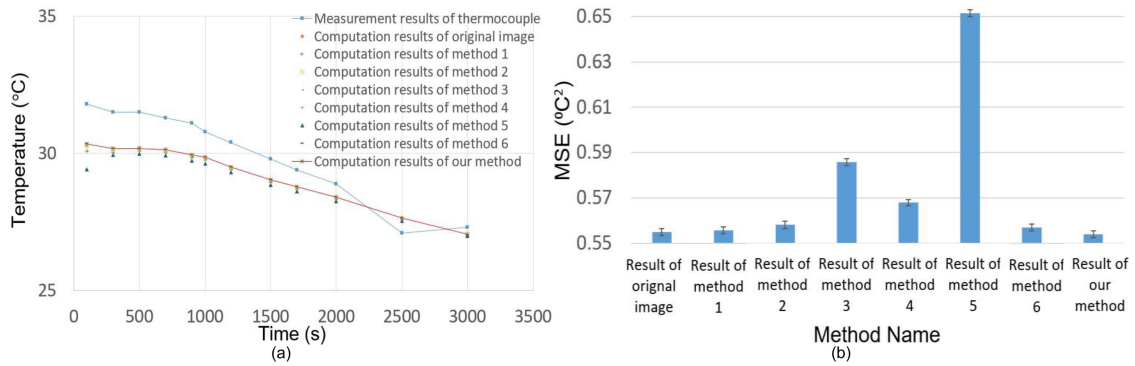| Graduation number	Working scope (°C)	Measurement precision (°C)	Measurement uncertainty [29]
E type (nickel-chrome and copper-nickel)	-200~900	0.1 (within ± 40 °C)	± 0.75%

Fig. 9. The results of temperature estimation experiment. (a) The temperature comparisons of thermocouple measurement result and the DHM estimation results using different ISN reduction methods. (b) The RMSE results of the original image and the DHM estimations using different ISN reduction methods.

result between the measured value and the computed value; (b) presents the corresponding mean squared error (MSE). The computational method of MSE is shown in (23), and it can evaluate the squared temperature error between the measurement value and the computation value from the statistics point of view. Regarding Fig. 9(a), the measurement result of thermocouple is marked by the blue squares and lines. The best computational result, i.e., the result using our proposed denoising method, is also labelled by the red stars and lines. A measurement result with big error happens when the time point is 2500s; this may come from the abnormal electromagnetic interference problem. The error analysis results of Fig. 9(a) are presented in Table 4. In this experiment, even we can repeat the measurement step for many times; however the temperature is a variable to the time and it changes all the time. That indicates we cannot know when we should read the result of thermocouple to get any our expected temperatures. Therefore in this experiment state we cannot get the multiple observation values of the expected temperature by the thermocouple actually. As a result, we only illustrate its measurement performance by Table 3. Another fact is, as we have stated above, the temperature in the same height should have the same value after the heating and the refrigeration controls; thus we can use the pixels sampled in the same height with the thermocouple to estimate the computational result of deionized water temperature. Ideally, the temperature estimation result of these pixels should be equal to the temperature measurement result of thermocouple. In this paper, we sample 2651 pixels which locate in the same height with the thermocouple to carry out the error analysis task (see Table 4). In Table 4, among 12 results our method can get 10 best calculation results which are marked in boldface; and the method 1 and the method 6 can also get the best computation results when the time points are 300s and 1200s, respectively. Clearly, the measurement value of thermocouple also has error; therefore a statistic assessment is performed in Fig. 9(b) furtherly. In Fig. 9(b) the statistical error is assessed by considering all the measurement and the computation results. From Fig. 9(b), our proposed method can get the best processing effect. Another problem is: the temperature differences among our proposed method and other method look small in Fig. 9 and Table 4, is it useful? The answer is positive. When researching the temperature jump process in the microgravity environment [28], the precise estimation of temperature field is really important.

$$MSE = \frac{\sum_{i=1}^{N} (X_{mes,i} - X_{com,i})^2}{N} \tag{23}$$

where $X_{mes,i}$ is the measurement data; $X_{com,i}$ is the computation data; N is the amount of the measurement value or the computation value, $N = 12$.

TABLE 4

The Error Performances (Mean±standard error∗) of Thermocouple System and DHM Denoising
Methods in Fig. 9(a)

Point ID	$Tt^{\#}$	Original image	Method 1	Method 2	Method 3	Method 4	Method 5	Method 6	Our Method
1	31.8	30.29503 ±0.00375	30.28637 ±0.00382	30.23855 ±0.00451	30.08784 ±0.00181	30.06596 ±0.00373	29.42521 ±0.00270	30.34580 ±0.00337	**30.34637 ±0.00369**
2	31.5	30.17863 ±0.00270	**30.17345 ±0.00266**	30.13508 ±0.00326	30.03293 ±0.00153	30.03795 ±0.00213	29.94576 ±0.00161	30.16933 ±0.00236	30.17120 ±0.00264
3	31.5	30.18681 ±0.00172	30.18424 ±0.00168	30.15503 ±0.00239	30.07707 ±0.00108	30.08912 ±0.00180	29.98840 ±0.00155	30.18723 ±0.00161	**30.18871 ±0.00167**
4	31.3	30.13130 ±0.00116	30.12838 ±0.00119	30.11554 ±0.00160	30.01217 ±0.00081	30.03721 ±0.00191	29.91476 ±0.00123	30.13104 ±0.00111	**30.13125 ±0.00113**
5	31.1	29.93907 ±0.00070	29.93945 ±0.00066	29.93468 ±0.00100	29.85321 ±0.00061	29.84580 ±0.00196	29.72679 ±0.00175	29.94853 ±0.00061	**29.94893 ±0.00067**
6	30.8	29.86078 ±0.00069	29.85864 ±0.00069	29.84431 ±0.00104	29.76009 ±0.00057	29.76099 ±0.00180	29.63911 ±0.00139	29.86470 ±0.00068	**29.86482 ±0.00067**
7	30.4	29.50362 ±0.00048	29.50136 ±0.00049	29.49161 ±0.00085	29.39687 ±0.00045	29.40736 ±0.00179	29.30565 ±0.00170	**29.50551 ±0.00057**	29.50457 ±0.00046
8	29.8	29.03280 ±0.00031	29.03434 ±0.00030	29.02560 ±0.00052	28.94471 ±0.00038	28.93669 ±0.00175	28.84178 ±0.00208	29.03893 ±0.00034	**29.03895 ±0.00030**
9	29.4	28.76987 ±0.00025	28.76882 ±0.00024	28.78808 ±0.00033	28.72227 ±0.00022	28.70764 ±0.00176	28.61136 ±0.00182	28.79026 ±0.00025	**28.79144 ±0.00024**
10	28.9	28.40230 ±0.00026	28.40368 ±0.00027	28.39329 ±0.00046	28.31756 ±0.00038	28.34493 ±0.00116	28.24792 ±0.00172	28.40983 ±0.00026	**28.41024 ±0.00025**
11	27.1	27.63534 ±0.00019	27.63793 ±0.00017	27.64310 ±0.00027	27.57612 ±0.00018	27.60251 ±0.00114	27.53801 ±0.00133	27.64843 ±0.00018	**27.64926 ±0.00019**
12	27.3	27.02575 ±0.00022	27.03049 ±0.00020	27.04530 ±0.00016	26.95616 ±0.00034	26.99606 ±0.00087	26.98283 ±0.00149	27.04533 ±0.00009	**27.04556 ±0.00021**

∗The standard error is calculated by dividing the standard deviation by the square root of number of measurements.

#Symbol Tt means the measurement temperature value of thermocouple.

3.3 Discussions

The DHM system has been used for fluid field estimation and measurement for many years. The traditional system always chooses to use the CCD sensor to construct its optical receiver because of its high imaging quality, low image distortion, and long service life, etc. Recently, the CMOS sensor is considered for the DHM application [30]. Comparing with the CCD sensor, the cost of CMOS sensor is really cheaper. This merit is an important design factor for the aerospace

application. After all the screening of the qualified component will always need to prepare enough candidates which will cost lots of funding. Another reason of selecting the CMOS sensor lies in that it has faster data processing speed and low power consumption which can also fulfill the in-orbit application request well. Because of the working principle and the manufacturing process problem, more noises will be observed from the CMOS sensor including the ISNs discussed in this paper and other speckle noises, etc. Clearly, the effective noise reduction [31] should be performed to get the high and the correct imaging details for the following computations. After a careful analysis and simulation of the optic path of the CMOS sensor-based DHM system, we think the ISNs mainly come from the complex interference of the input beams and their reflection ones which are mainly created from the unparallel assembly of the optic filter and the CMOS sensor. The micro distortions of optic components and coatings also contribute to that degradation [32] to some extent. From the image processing point of view, the image quality metrics can be used to represent the noise contamination degree of digital holographic image. The good image quality indicates the high imaging contrast, the abundant imaging details, and the low imaging noise. After a series of tests, some image features of GLCM are selected to carry out the image quality analysis because they can represent the imaging effect comprehensively.

An ISN reduction technique is developed in this paper for our CMOS sensor-based DHM system. Because the application of the optic coating technique and the optic filter, more complex interference phenomena can be observed. For the sake of simpleness, the case of unparallel assembly of optic filter and CMOS sensor is simulated and tested in this paper. Fig. 10(a) presents a simplified equivalent sketch map of that case. Its corresponding model can be defined in Equation (24). In Fig. 10(a), because the existence of included angle, the reflection beam of object beam (the violet solid line) will be prominent; similarly, the reflection beam of the reference beam (the green solid line) will also be observed. Clearly, if the included angle is zero, the reflection beam of object beam will be perpendicular to the CMOS sensor, and the reflection beam of the reference beam will be parallel to the reference beam itself. In our application, four beams will take part in the interference, they are the object beam (the red solid line), the reflection beam of object beam, the reference beam (the blue solid line), and the reflection beam of reference beam. The intensities of all the reflection beams are set by 10% of their individual input beams. Fig. 10(b) presents some actual examples of ISN and normal interference stripe which are recorded in the temperature estimation experiment of deionized water. From these results, the ISNs have different intensities and directions. To evaluate the robustness of our ISN reduction method, a series of simulated ISNs and normal interference stripes are created. In Fig. 10(c) and (d) show the simulated images with different ISNs. Regarding (c), the included angle between the optic filter and the CMOS sensor is tuned consecutively to create ISNs with different stripe directions; as for (d), the reflectivity of optic filter is controlled serially to create ISNs with different stripe intensities. Fig. 10(e) and (f) show the image quality evaluation results of the images in (c) and (d), respectively. From (e) and (f), the changes of GLCM features are not remarkable except for the minor results of average gradient and contrast. These results can illustrate the robustness of our proposed method to some extent.

$$I_{pra}(x, y) = \left| O(x, y) + R(x, y) + O_{ref}(x, y) + R_{ref}(x, y) \right|^2 \tag{24}$$

where $I_{pra}(x, y)$ is the practical holographic imaging result; $O_{ref}(x, y)$ and $R_{ref}(x, y)$ are the equivalent reflecting results of the object and the reference beams, respectively.

Our algorithm performance is also evaluated in the frequency domain. First, we compare the frequency spectrum before and after the application of proposed denoising technique. Fig. 11(a), (b), (c) and (d) present the corresponding image and results: (a) is the original simulated interference stripe with ISN, (b) is the frequency spectrum of (a); (c) is the denoising result of (a) using our proposed method; and (d) is the frequency spectrum of (c). The signal components are marked by the red circles and the main noise components are labeled by the yellow circles in (b) and (d), respectively. After a careful check of the frequency spectrums it can be found that all the frequency spectrum data are still remained even after the denoising, and only their intensities decrease to some extent. The decreasing degree of ISN is larger than that of the
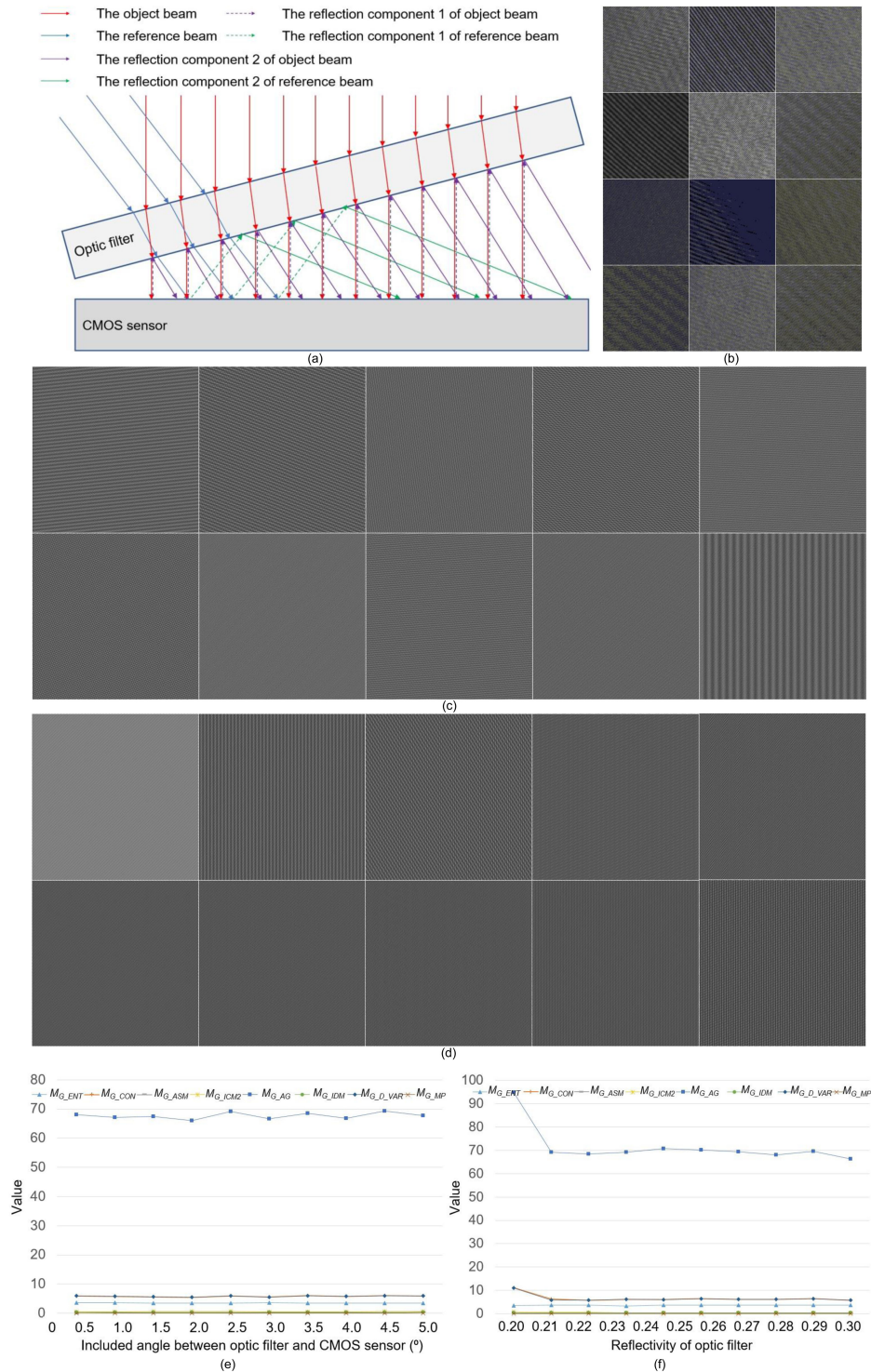
Fig. 10. The ISN generative model, the actual ISN imaging samples, the simulated ISN imaging samples; and the computation robustness evaluation results of image quality metrics considering different included angles and reflectivity indices. (a) The generative sketch map of the unparallel assembly-caused interference phenomenon. (b) The actual interference stripe samples recorded from the temperature measurement experiment of deionized water. (c) The simulated interference images using different included angles between optic filter and CMOS sensor. The image size is 500 × 500, the reflectivity of optic filter is 0.2. (d) The simulated interference images using different reflectivities of optic filter. The image size is 500 × 500, the included angle is 5°. (e) The GLCM features evaluation results of (c). (f) The GLCM features evaluation results of (d).
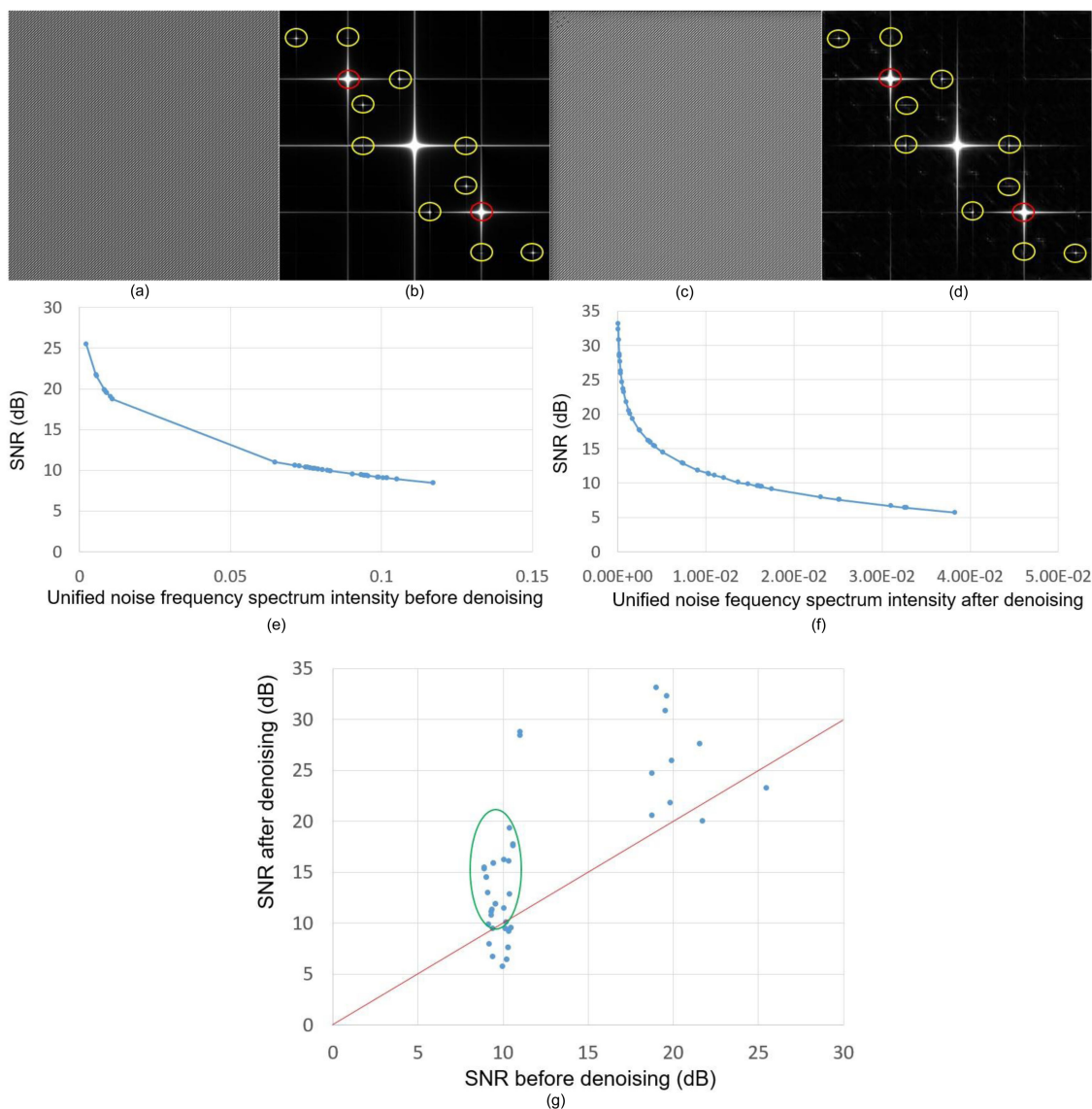
Fig. 11. The frequency spectrum analysis experiment of proposed denoising method. (a) The original simulation image, where the image size is 500 × 500, the reflectivity of optic filter is 0.1, the included angle is 1°. (b) The frequency spectrum image of (a). (c) The denoising result image of (a) using our proposed denoising method. (d) The frequency spectrum image of (c). (e) The relationship between the frequency spectrum intensity and the SNR before our denoising. (f) The relationship between the frequency spectrum intensity and the SNR after our denoising. (g) The SNR relationship of the same frequency spectrum before and after our denoising.

interference stripe. This phenomenon can be explained: our proposed method does not belong to any high-pass, low-pass, or band-pass filters, no frequency spectrum can be removed completely by it; however it can compress the frequency spectrum intensity. Since the positions of frequency spectrum signal or noise cannot be changed, the width and the period of stripe will not influence the computation performance of our algorithm remarkably. Second, the unified noise frequency spectrum intensity before and after the application of our denoising method is investigated. Some simulated images are utilized. Regarding the CMOS sensor, most of its commercial products have a 90% transmittance and the included angle of optic filter cannot be too large; otherwise this sensor will be regarded as the unqualified product [33]. Based on these facts, we can simulate a series

of images by Equation (24), where the reflectivity is set by 0.1 and the included angle belongs to [-5, +5]. Then we can build the relationship between the unified noise frequency spectrum intensity and the processing effect index of denoising method to assess our algorithm. The unified noise frequency spectrum intensity is calculated by the ratio between the center intensity of noise component and that of the signal in the central 0 level. A signal noise ratio (SNR) index is estimated to evaluate the denoising effect of our algorithm, and it can be computed by the ratio between the center intensity of signal component in +1 level and that of the noise component (see the red and yellow circles in Fig. 11(c) and (d)). Fig. 11(e) and (f) illustrate the corresponding results. In (e), fifty unified noise frequency spectrum intensities are computed before denoising and their corresponding SNR values are also calculated. Then the unified noise frequency spectrum intensity is presented in the abscissa according to the order of small to large, and the corresponding SNRs are also given out in the ordinate. Similarly, the data after denoising can be labeled in (f). From (e) and (f), the SNR will increase with the decrease of unified noise frequency spectrum intensity in their individual experiment state. Clearly, the larger the unified noise frequency spectrum intensity is, the stronger the ISN in the spatial domain will be. Third, a computational effect evaluation method of proposed algorithm is studied. In this experiment, we compare the relationship of SNR before and after the denoising processing. Fig. 11(g) illustrates the corresponding results. In (g), we mark a red line and a green ellipse in that figure. From this figure it can be seen: if the SNR cannot be improved after the denoising, the blue points will locate lower than that red line; in this situation, we think the performance of proposed algorithm is not good. Another fact is, if the SNR is too small, the final temperature estimation error [34] may also be high; therefore the processing effect of proposed denoising method is unreliable. For example, if the SNR after denoising is still lower than 19 dB, i.e., the blue point locates in the green ellipse, in that situation we do not recommend to use this algorithm to carry out the denoising task.

4. Conclusion

An ISN reduction method of the CMOS sensor-based DHM system is proposed. Comparing with the application of CCD sensor, the CMOS sensor will use more optic components to improve its imaging quality which may cause the ISN problem. Both the additive noise and the multiplicative noise processing methods are designed. First, the Laplacian pyramid is used to highlight the ISN and protect the normal interference stripe. Second, the cartoon-texture decomposition is performed to reduce the additive ISN. Third, the upsampling of Laplacian pyramid is carried out to the texture part. Finally, an improved Lee filtering is employed to decrease the multiplicative ISN noise. Two experiments are performed to assess the validity of proposed method, i.e., the image quality evaluation experiment and the temperature estimation experiment of deionized water. The corresponding experiment results have illustrated the effectiveness of proposed method and it is fit for solving a deionized water temperature estimation application where the texture complexity of target image is relatively low. The simulated ISN images are also used to test the robustness of proposed method. In future, more theory analyses of DHM optic path, such as the distortions of optic components and their coupling problem will be modelled; and the corresponding fast computational method will be developed for the researches in the space station.

Acknowledgment

References

[1] D. Deng and W. Qu, "Fast aberrations compensation in digital holographic microscopy based on phase transformation," *IEEE Photon. J.*, vol. 12, no. 3, Jun. 2020, Art. no. 6901409.
[2] C. Wylock, S. Dehaeck, T. Cartage, P. Colinet, and B. Haut, "Experimental study of gas-liquid mass transfer coupled with chemical reactions by digital holographic interferometry," *Chem. Eng. Sci.*, vol. 66, no. 14, pp. 3400–3412, 2011.

[3] J. Xiong, Q. Fu, R. Idoughi, and W. Heidrich, "Reconfigurable rainbow PIV for 3D flow measurement," in *Proc. IEEE Int. Conf. Comput. Photography*, Pittsburgh, PA, USA, 2018, pp. 1–9.

[4] J. Di, Y. Li, K. Wang, and J. Zhao, "Quantitative and dynamic phase imaging of biological cells by the use of the digital holographic microscopy based on a beam displacer unit," *IEEE Photon. J.*, vol. 10, no. 4, Aug. 2018, Art. no. 6900510.

[5] G. Cossu, A. Sturniolo, and E. Ciaramella, "Modelization and characterization of a CMOS camera as an optical real-time oscilloscope," *IEEE Photon. J.*, vol. 12, no. 6, Dec. 2020, Art. no. 7906313.

[6] E. Artyomov, Y. Rivenson, G. Levi, and O. Yadid-Pecht, "Morton (Z) scan based real-time variable resolution CMOS image sensor," *IEEE Trans. Circuits Syst. Video Technol.*, vol. 15, no. 7, pp. 947–952, Jul. 2005.

[7] D. Deng, W. Qu, W. He, Y. Wu, X. Liu, and X. Peng, "Phase retrieval for digital holographic microscopy with defocused holograms," *IEEE Photon. J.*, vol. 10, no. 1, Feb. 2018, Art. no. 6900209.

[8] T. Du, Y. Kong, X. Qian, W. Ding, and Z. Wang, "Suppression of speckle noise in digital holography with spatial and temporal domain, depolarization," *IEEE Access*, vol. 8, pp. 22266–22274, 2020.

[9] C. Cho, B. Choi, H. Kang, and S. Lee, "Laplace operation-based DC noise reduction in digital holography," *IEEE Photon. Technol. Lett.*, vol. 25, no. 12, pp. 1188–1191, Jun. 2013.

[10] Y. Mori, and T. Nomura, "Speckle reduction in hologram generation based on spherical waves synthesis using low-coherence digital holography," *J. Display Technol.*, vol. 11, no. 10, pp. 867–872, 2015.

[11] C. Shen, X. Bao, J. Tan, S. Liu, and Z. Liu, "Two noise-robust axial scanning multi-image phase retrieval algorithms based on pauta criterion and smoothness constraint," *Opt. Exp.*, vol. 25, no. 14, pp. 16235–16231–16235–15, 2017.

[12] X. Cai, "Reduction of speckle noise in the reconstructed image of digital holography," *Optik*, vol. 121, pp. 394–399, 2010.

[13] W. Jeong, K. Son, J. Cho, H. Yang, and N.-C. Park, "Suppression algorithm of speckle noise for parallel phase-shift digital holography," *Opt. Laser Technol.*, vol. 112, pp. 93–100, 2019.

[14] B. Guan *et al.*, "CMOS compatible reconfigurable silicon photonic lattice filters using cascaded unit cells for RF-photonic processing," *IEEE J. Sel. Topics Quantum Electron.*, vol. 20, no. 4, pp. 8202110–16231–8202110–10, Jul./Aug. 2014.

[15] T. Kakue *et al.*, "Parallel phase-shifting digital holography capable of simultaneously capturing visible and invisible three-dimensional information," *J. Display Technol.*, vol. 6, no. 10, pp., 2010. pp. 472–478.

[16] J. Zhou, D. Zhang, P. Zou, W. Zhang, and W. Zhang, "Retinex-based Laplacian pyramid method for image defogging," *IEEE Access*, vol. 7, pp. 122459–122472, 2019.

[17] A. Buades, T. M. Le, J.-M. Morel, and L. A. Vese, "Fast cartoon + texture image filters," *IEEE Trans. Image Process.*, vol. 19, no. 8, pp. 1978–1986, Aug. 2010.

[18] Y. Zhou, J. Cheng, T. Liu, Y. Wang, H. Deng, and Y. Xiong, "GPU-based SAR image lee filtering," in *Proc. IEEE Int. Conf. Comput. Sci. Netw. Technol.*, Dalian, China, 2019, pp. 17–21.

[19] Z. Sun, Z. Zhang, Y. Chen, S. Liu, and Y. Song, "Frost filtering algorithm of SAR images with adaptive windowing and adaptive tuning factor," *IEEE Geosci. Remote Sens. Lett.*, vol. 17, no. 6, pp. 1097–1101, Jun. 2020.

[20] N. S. Anand, R. Marappan, and G. Sethumadhavan, "Performance analysis of SAR image speckle filters and its recent challenges," in *Proc. IEEE Int. Conf. Comput. Intell. Comput. Res.*, Madurai, India, 2018, pp. 1–4.

[21] J.-S. Lee, J.-H. Wen, T. L. Ainsworth, K.-S. Chen, and A. J. Chen, "Improved sigma filter for speckle filtering of SAR imagery," *IEEE Trans. Geosci. Remote Sens.*, vol. 47, no. 1, pp. 202–213, Jan. 2009.

[22] S. D. Nicola, A. Finizio, G. Pierattini, P. Ferraro, and D. Alfieri, "Angular spectrum method with correction of anamorphism for numerical reconstruction of digital holograms on tilted planes," *Opt. Exp.*, vol. 13, no. 24, pp. 9935–9940, 2005.

[23] C. O. Dumitru and M. Datcu, "Information content of very high resolution SAR images: Study of feature extraction and imaging parameters," *IEEE Trans. Geosci. Remote Sens.*, vol. 51, no. 8, pp. 4591–4610, Aug. 2013.

[24] G. Xu, Q. Liu, J. Qin, and Z. Zhu, "Numerical study of thermocapillary-buoyancy convection of volatile liquid layer in an enclosed cavity," *Microgr. Sci. Technol.*, vol. 32, pp. 305–319, 2020.

[25] A. N. Bashkatov and E. A. Genina, "Water refractive index in dependence on temperature and wavelength: A simple approximation," in *Proc. Int. Soc. Opt. Eng.*, Saratov, Russia, 2003, pp. 393–395, vol. 5068.

[26] Q. Wen *et al.*, "Temperature coefficients of the refractive index for complex hydrocarbon mixtures," *Int. J. Thermophys.*, vol. 5, pp. 930–941, 2014.

[27] I. N. Bronshtein, K. A. Semendyayev, G. Musiol, and H. Muhlig, *Handbook of Mathematics*, 5th ed., Berlin Heidelberg, Germany: Springer-Verlag, 2007.

[28] C. A. Ward, and F. Duan, "Turbulent transition of thermocapillary flow induced by water evaporation," *Phys. Rev. E*, vol. 69, no. 5, pp. 056308–16231–056308–10, 2004.

[29] V. Witkovsky, G. Wimmer, Z. Durisova, S. Duris, and R. Palencar, "Brief overview of methods for measurement uncertainty analysis: GUM uncertainty framework, Monte Carlo method, characteristic function approach," in *Proc. Int. Conf. Meas.*, Smolenice, Slovakia, 2017, pp. 35–38.

[30] A. A. Sevruygin, S. A. Pulkin, I. M. Tursunov, D. V. Venediktov, and V. Yu. Venediktov, "Digital correction of distortions in holographic interferometer," in *Proc. Int. Conf. Laser Opt.*, St. Petersburg, Russia, 2016, pp. R4–R5.

[31] H. Liu, S. Yang, C. Guo, J. Li, M. Yan, and J. Lan, "Calibration of imaging sensor and fiber optic taper-caused distortion in an X-ray intensified CMOS camera," *IEEE Access*, vol. 7, pp. 185393–185407, 2019.

[32] Z. Jiang, X. Pan, X. He, Y. Kong, S. Wang, and C. Liu, "Phase retrieval of on-axis digital holography with modified coherent diffraction imaging," *IEEE Photon. J.*, vol. 12, no. 6, 2020, Art. no. 6901712.

[33] J. Li, and Y. Wu, *Diffraction Calculation and Digital Holography I*. Beijing, China: Science Press, 2016.

[34] M. F. Schatz and G. P. Neitzel, "Experiments on thermocapillary instabilities," *Annu. Rev. Fluid Mech.*, vol. 33, no. 1, pp. 93–127, 2001.